nature astronomy

Supplementary information https://doi.org/10.1038/s41550-026-02939-x

Vigorous turbulence driven by quasar-mode feedback in a cluster core

In the format provided by the authors and unedited

Supplementary Information

Basic properties of H1821+643 and other clusters. To highlight the distinctive properties of H1821+643 compared to other clusters, we summarised key physical parameters of each cluster and its central AGN in Supplementary Table. 1. These included the 2–10 keV X-ray luminosity of the cool core ($L_{\rm cool}$), its radius ($r_{\rm cool}$) [1, 2], absorption-corrected 2–10 keV AGN luminosity ($L_{\rm AGN,X}$) [3–6], mechanical energy ($E_{\rm cav}$) and power ($P_{\rm cav}$) of X-ray cavities [1, 7–10], 1.4 GHz radio luminosity ($L_{1.4\rm GHz}$) as a tracer of jet activity [2, 3] and mass of the central SMBH ($M_{\rm BH}$) [11–14].

The 2–10 keV AGN luminosity of H1821+643 exceeded that of other clusters by more than 1–5 orders of magnitude, making it exceptional. Previous studies have shown that the bolometric-to-X-ray luminosity ratio ($L_{\rm bol}/L_{\rm AGN,X}$) is typically $\sim$20 and increases with $L_{\rm AGN,X}$ [15, 16], implying an even stronger bolometric output in luminous quasars. The bolometric luminosity of H1821+643, estimated as $50L_{\rm AGN,X}$ [1], was consistent with independent multiwavelength spectral-energy-distribution fits [17]. H1821+643 accreted at an Eddington ratio of $\lambda_{\rm Edd} \sim 0.3$–$0.6$, typical of quasar-mode systems, whereas other clusters typically exhibited $\lambda_{\rm Edd} \sim 0.01$ or lower.

Velocity dispersion and non-thermal energy fraction. In nearby clusters with less luminous AGNs, XRISM and Hitomi observations showed ICM velocity dispersions of $\lesssim$160 km s^{-1} within the central $\lesssim$100 kpc (Perseus [18, 19], Abell 2029 [20, 21], Hydra A [22], Virgo [23], Ophiuchus [24] and Centaurus [4]). In comparison, Cygnus A [25] and H1821+643 exhibit substantially higher velocity dispersions of $\sim$250–300 km s^{-1} at $kT \sim 6$ keV.

We note that the XRISM observations of the Virgo cluster indicate elevated velocity dispersions only within the innermost few kpc (<4.65 kpc) and at low temperatures (<2 keV), corresponding to the cold ICM phase [23]. This very narrow region probes physical conditions distinct from the hot (>2 keV) ICM on larger scales, and we therefore treat it as an exception not included in our main comparison on $\sim$100 kpc scales. Measurements at larger radii ($\sim$5–25 kpc) in Virgo are included in our comparison. Similarly, in Cygnus A, a velocity dispersion of $\sim$440 km s^{-1} has been reported within the central <35 kpc [25], corresponding to the cold ICM ($\lesssim$2 keV) and thus not directly comparable to the hot ICM on $\sim$100 kpc scales. For the hot ICM ($kT \sim 5.5$ keV), a velocity dispersion of $\sim$260 km s^{-1} has been reported; in this powerful FR II radio galaxy, this is likely associated with bulk motions driven by the expansion of radio cocoons rather than isotropic turbulence [26].

The non-thermal-to-thermal energy fraction, $f_{\rm nth}$, was estimated from the line-of-sight velocity dispersion by assuming isotropic turbulence or velocity shear, $\sigma_{\rm 3D} = \sqrt{3}\sigma_v$. The resulting non-thermal pressure is then compared with the thermal pressure using $f_{\rm nth} \simeq (1/3)\mu m_p \sigma_{\rm 3D}^2/kT$, where $\mu \simeq 0.61$ is the mean molecular weight per particle (electrons plus ions) [27]. This yields $f_{\rm nth} \sim 8.4\%$ in H1821+643, substantially higher than in the other clusters. Whereas clusters with $L_{\rm X,AGN} \lesssim 10^{45}$ erg s^{-1} show no clear dependence of $f_{\rm nth}$ on AGN X-ray luminosity, with H1821+643 standing out (Fig. 3 and Supplementary Fig. 1).

Examining $f_{\rm nth}$ as a function of projected radius, H1821+643 exhibits the most vigorous gas motions among well-studied systems at comparable spatial scales, including Hydra A (with powerful jets) [22] and the cool-core cluster Abell 2029 [21]. In other clusters where measurements extend to larger radii ($\gtrsim$100 kpc), $f_{\rm nth}$ generally decreases. Clusters with lower $L_{\rm X,AGN}$, such as Centaurus [4] and Ophiuchus [24], are typically measured only within their innermost cores. At similar radii, the data tentatively suggest that $f_{\rm nth}$ increases with AGN luminosity (Supplementary Fig. 2).

Supplementary Table 1: **Basic properties of the clusters in our sample.**

Note. Key properties of the clusters and their central AGN are listed. Columns include the 2–10 keV luminosity ($L_{\rm cool}$) and radius of the cool core ($r_{\rm cool}$) [1, 2], intrinsic 2–10 keV AGN luminosity ($L_{\rm AGN,X}$) [3–6], mechanical energy ($E_{\rm cav}$) and power of X-ray cavities ($P_{\rm cav}$) [1, 7, 8, 10], 1.4 GHz radio luminosity ($L_{\rm 1.4GHz}$) [2, 3], and central SMBH mass ($M_{\rm BH}$) [11, 12, 14].

Cluster name	$L_{\rm cool}$ (10^{42} erg s^{-1})	$r_{\rm cool}$ (kpc)	$L_{\rm AGN,X}$ (10^{42} erg s^{-1})	$E_{\rm cav}$ (10^{58} erg)	$P_{\rm cav}/L_{\rm 1.4GHz}$ (10^{42} erg s^{-1})	$M_{\rm BH}$ ($10^9 M_\odot$)
H1821+643	$\approx$3500	90	4200^{+100}_{-100}	60	700/3.2	3.0
Cygnus A	293^{+3}_{-3}	92	173^{+29}_{-19}	84	1300/152.9	2.7
Perseus	545^{+2}_{-2}	110	25^{+54}_{-17}	19	150/0.24	0.34
Abell 2029	1049^{+5}_{-5}	127	$2.1^{+0.2}_{-0.2}$	4.8	87/0.15	4.0
Hydra A	227^{+2}_{-2}	107	$1.0^{+0.1}_{-0.1}$	900	2000/4.21	5.8
Virgo	$6.3^{+0.1}_{-0.1}$	39	$0.051^{+0.003}_{-0.003}$	0.5	13/0.081	6.5
Ophiuchus	324^{+1}_{-2}	83	<0.33	5000	$\cdots$/0.00072	6.9
Centaurus	$22.0^{+0.1}_{-0.1}$	87	<0.012	0.06	7.4/0.016	2.0

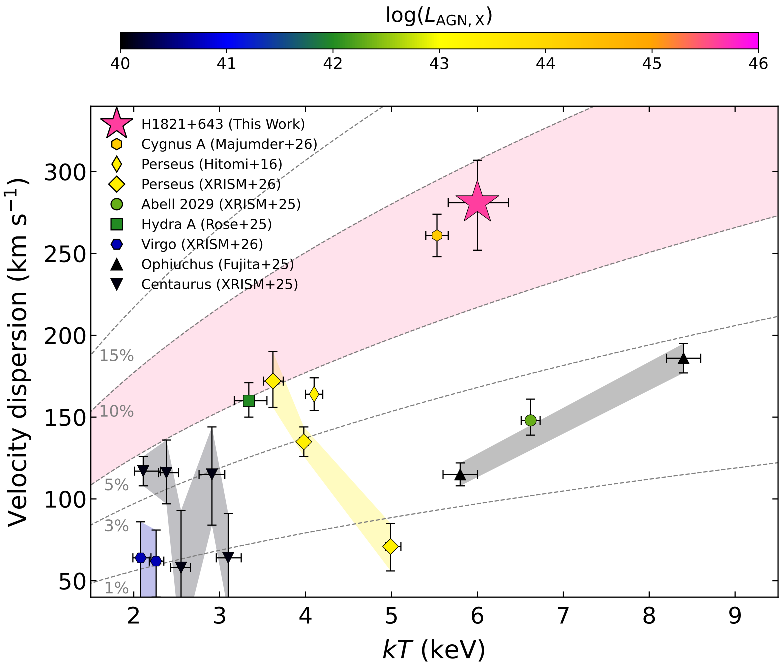

Supplementary Fig. 1: **Velocity dispersion of the ICM within 100 kpc scales as a function of plasma temperature.** Individual measurements for H1821+643, Cygnus A, Perseus, Abell 2029, Hydra A, Virgo, Ophiuchus and Centaurus clusters are shown for the hot (>2 keV) ICM. The symbol colour indicates the 2–10 keV AGN luminosity ($L_{\mathrm{X,AGN}}$) as shown by the colour bar. For clusters with multiple measurements at different regions, the corresponding ranges are indicated by shaded areas. Error bars represent 1σ uncertainties. Dashed curves indicate combinations of temperature and velocity dispersion corresponding to non-thermal energy fractions f_{nth} of 1%, 3%, 5%, 10% and 15%. H1821+643 is the only cluster located in the $f_{\mathrm{nth}} \sim 5$–10% regime (pink shaded region).

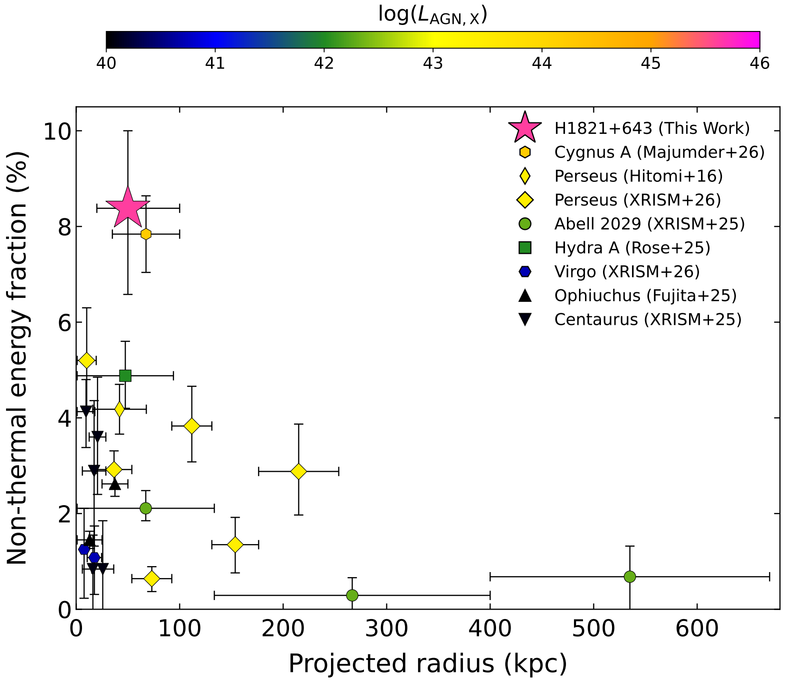

Supplementary Fig. 2: **Radial distribution of the non-thermal energy fraction in the ICM.** The fraction of non-thermal energy, $f_{\rm nth}$, is shown as a function of projected radius. Individual measurements for H1821+643, Cygnus A, Perseus, Abell 2029, Hydra A, Virgo, Ophiuchus and Centaurus clusters are included for the hot (>2 keV) ICM. The symbol colour indicates the 2–10 keV AGN luminosity ($L_{\rm X,AGN}$) as shown by the colour bar. Different marker types distinguish individual measurements. Horizontal bars indicate the projected radial ranges, while vertical error bars represent 1σ uncertainties.

References

[1] Russell, H. R. *et al.* A cooling flow around the low-redshift quasar H1821+643. *Mon. Not. R. Astron. Soc.* **528**, 1863–1878 (2024).

[2] Bîrzan, L. *et al.* The duty cycle of radio-mode feedback in complete samples of clusters. *Mon. Not. R. Astron. Soc.* **427**, 3468–3488 (2012).

[3] Hlavacek-Larrondo, J. *et al.* The rapid evolution of AGN feedback in brightest cluster galaxies: switching from quasar-mode to radio-mode feedback. *Mon. Not. R. Astron. Soc.* **431**, 1638–1658 (2013).

[4] XRISM Collaboration *et al.* The bulk motion of gas in the core of the Centaurus galaxy cluster. *Nature.* **638**, 365–369 (2025).

[5] Russell, H. R. *et al.* Radiative efficiency, variability and Bondi accretion on to massive black holes: the transition from radio AGN to quasars in brightest cluster galaxies. *Mon. Not. R. Astron. Soc.* **432**, 530–553 (2013).

[6] Pérez-Torres, M. A. *et al.* The origin of the diffuse non-thermal X-ray and radio emission in the Ophiuchus cluster of galaxies. *Mon. Not. R. Astron. Soc.* **396**, 2237–2248 (2009).

[7] Rafferty, D. A., McNamara, B. R., Nulsen, P. E. J. & Wise, M. W. The Feedback-regulated Growth of Black Holes and Bulges through Gas Accretion and Starbursts in Cluster Central Dominant Galaxies. *Astrophys. J.* **652**, 216–231 (2006).

[8] Nulsen, P. E. J., McNamara, B. R., Wise, M. W. & David, L. P. The Cluster-Scale AGN Outburst in Hydra A. *Astrophys. J.* **628**, 629–636 (2005).

[9] Forman, W. *et al.* Partitioning the Outburst Energy of a Low Eddington Accretion Rate AGN at the Center of an Elliptical Galaxy: The Recent 12 Myr History of the Supermassive Black Hole in M87. *Astrophys. J.* **844**, 122 (2017).

[10] Giacintucci, S. *et al.* Discovery of a Giant Radio Fossil in the Ophiuchus Galaxy Cluster. *Astrophys. J.* **891**, 1 (2020).

[11] Shapovalova, A. I. *et al.* First Long-term Optical Spectral Monitoring of a Binary Black Hole Candidate E1821+643. I. Variability of Spectral Lines and Continuum. *Astrophys. J. Suppl.* **222**, 25 (2016).

[12] McNamara, B. R., Rohanizadegan, M. & Nulsen, P. E. J. Are Radio Active Galactic Nuclei Powered by Accretion or Black Hole Spin? *Astrophys. J.* **727**, 39 (2011).

[13] Event Horizon Telescope Collaboration *et al.* First M87 Event Horizon Telescope Results. I. The Shadow of the Supermassive Black Hole. *Astrophys. J. Lett.* **875**,

L1 (2019).

[14] Arzoumanian, Z. *et al.* The NANOGrav 11 yr Data Set: Limits on Supermassive Black Hole Binaries in Galaxies within 500 Mpc. *Astrophys. J.* **914**, 121 (2021).

[15] Vasudevan, R. V. & Fabian, A. C. Piecing together the X-ray background: bolometric corrections for active galactic nuclei. *Mon. Not. R. Astron. Soc.* **381**, 1235–1251 (2007).

[16] Duras, F. *et al.* Universal bolometric corrections for active galactic nuclei over seven luminosity decades. *Astron. & Astrophys.* **636**, A73 (2020).

[17] Gupta, K. K. *et al.* BASS: XLIII. Optical, UV, and X-ray emission properties of unobscured Swift/BAT active galactic nuclei. *Astron. & Astrophys.* **691**, A203 (2024).

[18] Hitomi Collaboration *et al.* The quiescent intracluster medium in the core of the Perseus cluster. *Nature.* **535**, 117–121 (2016).

[19] The Xrism Collaboration *et al.* Disentangling multiple gas kinematic drivers in the Perseus galaxy cluster. *Nature.* **650**, 309–313 (2026).

[20] Xrism Collaboration *et al.* XRISM Reveals Low Nonthermal Pressure in the Core of the Hot, Relaxed Galaxy Cluster A2029. *Astrophys. J. Lett.* **982**, L5 (2025).

[21] Audard, M. *et al.* Constraining gas motion and non-thermal pressure beyond the core of the Abell 2029 galaxy cluster with XRISM. *Publ. Astron. Soc. Jpn* **77**, S242–S253 (2025).

[22] Rose, T. *et al.* XRISM Constrains Atmospheric Motion and Turbulent Dissipation in the Archetypal Radio-mode Feedback System Hydra-A. *Astrophys. J.* **990**, 42 (2025).

[23] Xrism Collaboration *et al.* A XRISM/Resolve View of the Dynamics in the Hot Gaseous Atmosphere of M87. *Astrophys. J.* **998**, 210 (2026).

[24] Fujita, Y., Fukushima, K., Sato, K., Fukazawa, Y. & Kondo, M. XRISM observation of the Ophiuchus galaxy cluster: Quiescent velocity structure in the dynamically disturbed core. *Publ. Astron. Soc. Jpn* **77**, S270–S275 (2025).

[25] Majumder, A. *et al.* Spectrally Resolved Gas Kinematics in Cygnus A: XRISM Detects AGN Jet-induced Velocity Dispersion in Multitemperature Gas. *Astrophys. J.* **998**, 160 (2026).

[26] Shirotori, M. & Fujita, Y. XRISM mock observations of simulated active galactic nucleus jets in the core of a galaxy cluster. *Publ. Astron. Soc. Jpn* **78**, 609–616 (2026).

[27] Truong, N. *et al.* X-ray-inferred kinematics of the core intracluster medium in Perseus-like clusters: Insights from the TNG-Cluster simulation. *Astron. & Astrophys.* **686**, A200 (2024).